LETTER

doi:10.1038/nature14356

Structures of actin-like ParM filaments show architecture of plasmid-segregating spindles

Tanmay A. M. Bharat[1], Garib N. Murshudov[1], Carsten Sachse[2] & Jan Löwe[1]

Active segregation of *Escherichia coli* low-copy-number plasmid R1 involves formation of a bipolar spindle made of left-handed double-helical actin-like ParM filaments[1–6]. ParR links the filaments with centromeric *parC* plasmid DNA, while facilitating the addition of subunits to ParM filaments[3,7–9]. Growing ParMRC spindles push sister plasmids to the cell poles[9,10]. Here, using modern electron cryomicroscopy methods, we investigate the structures and arrangements of ParM filaments *in vitro* and in cells, revealing at near-atomic resolution how subunits and filaments come together to produce the simplest known mitotic machinery. To understand the mechanism of dynamic instability, we determine structures of ParM filaments in different nucleotide states. The structure of filaments bound to the ATP analogue AMPPNP is determined at 4.3 Å resolution and refined. The ParM filament structure shows strong longitudinal interfaces and weaker lateral interactions. Also using electron cryomicroscopy, we reconstruct ParM doublets forming antiparallel spindles. Finally, with whole-cell electron cryotomography, we show that doublets are abundant in bacterial cells containing low-copy-number plasmids with the ParMRC locus, leading to an asynchronous model of R1 plasmid segregation.

Using electron cryomicroscopic (cryo-EM) images collected on a direct-electron detector, we performed real-space helical reconstruction to elucidate a 4.3 Å structure of ParM filaments assembled with the nucleotide AMPPNP (Fig. 1a–c and Extended Data Fig. 1, Extended Data Table 1 and Supplementary Video 1). Densities corresponding to α-helices, β-strands and many side chains were clearly observed (Fig. 1d–g). AMPPNP was also observed in our map as strong density, especially on the phosphates (Fig. 1h). No apparent resolution anisotropy was detected in the reconstruction (Extended Data Fig. 1), indicating that the entire ParM protein is rigidly held in the filament. To derive an atomic model of the ParM filament, a previous, monomeric crystal structure of ParM and AMPPNP bound to the tail of ParR (Protein Data Bank (PDB) accession code 4A62) was fitted into the map, and the filament model iteratively rebuilt and all-atom refined using stereochemical restraints with REFMAC.

Surprisingly, the two protofilaments (strands) making up the double-helical ParM filament are held together only by salt bridges (Fig. 2a, b, Extended Data Figs 2 and 3 and Extended Data Table 2). The ParM inter-protofilament interface is small (calculated interface area 371 Å^2) and does not resemble a canonical protein–protein interface containing a hydrophobic core. To demonstrate the validity of this assessment we mutated two positively charged residues within the inter-protofilament interface to aspartic acids (K258D, R262D) and tested what effect this had on the stability of ParM filaments. Filament formation (with AMPPNP) from the resulting mutant protein ParM (K258D, R262D) was inefficient (Extended Data Fig. 3g). The few filaments that were formed were unstable, and tended to be bent (Fig. 2c and Extended Data Fig. 3h). Reference-free class averaging of these filaments showed that even though most of the few observed filaments were double helical like wild-type ParM, some single-helical filaments were also present (Fig. 2d and Extended Data Fig. 3i). These observations indicate that although the interface between protofilaments in ParM is surprisingly small, it is sufficient for double-helical filament assembly since many identical contacts along the filament contribute to the overall binding energy. Different actin-like proteins show very different filament arrangements, from single (crenactin, possibly[11]) to parallel double helical (left-handed: ParM; right-handed: actin; and non-staggered: MamK[12]) and antiparallel, double straight

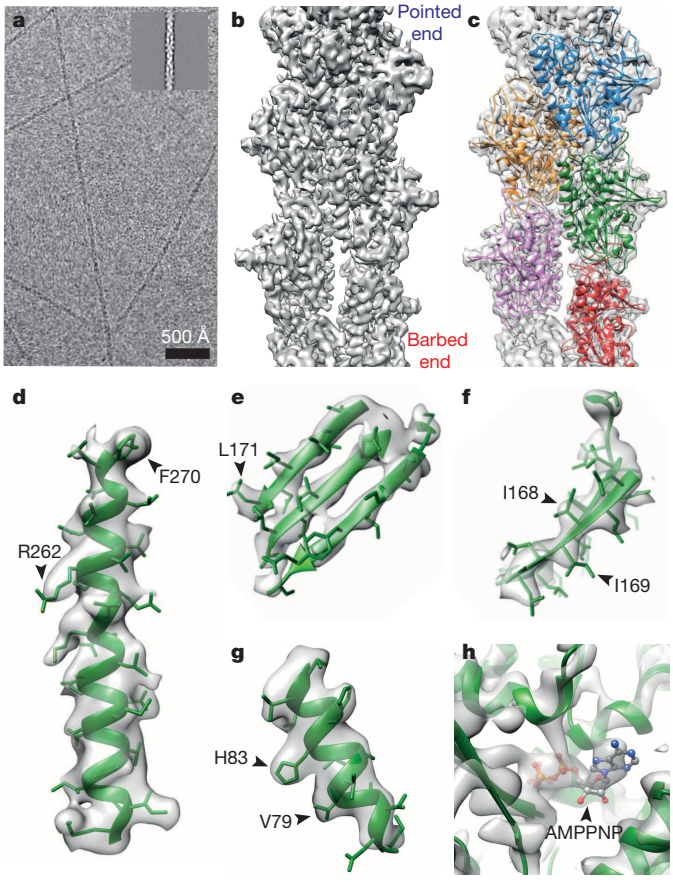

Figure 1 | Cryo-EM reconstruction at 4.3 Å of ParM+AMPPNP filaments. **a**, Cryo-EM image of ParM+AMPPNP filaments. Inset: class average. This experiment was repeated nine times. **b**, A 4.3 Å reconstruction of the filaments, isosurface contoured at 2σ away from the mean (see Extended Data Fig. 1 and Supplementary Video 1). **c**, The same reconstruction as **b**, overlaid with the refined atomic model with individual ParM subunits coloured differently. **d**–**g**, Enlarged regions of the cryo-EM map showing resolved secondary structure elements and side-chain densities, contoured at 1σ. **h**, Density for the nucleotide is stronger than that of the protein (contoured at 3σ).

[1]Structural Studies Division, MRC Laboratory of Molecular Biology, Francis Crick Avenue, Cambridge CB2 0QH, UK. [2]Structural and Computational Biology Unit, European Molecular Biology Laboratory, Meyerhofstrasse 1, Heidelberg 69117, Germany.

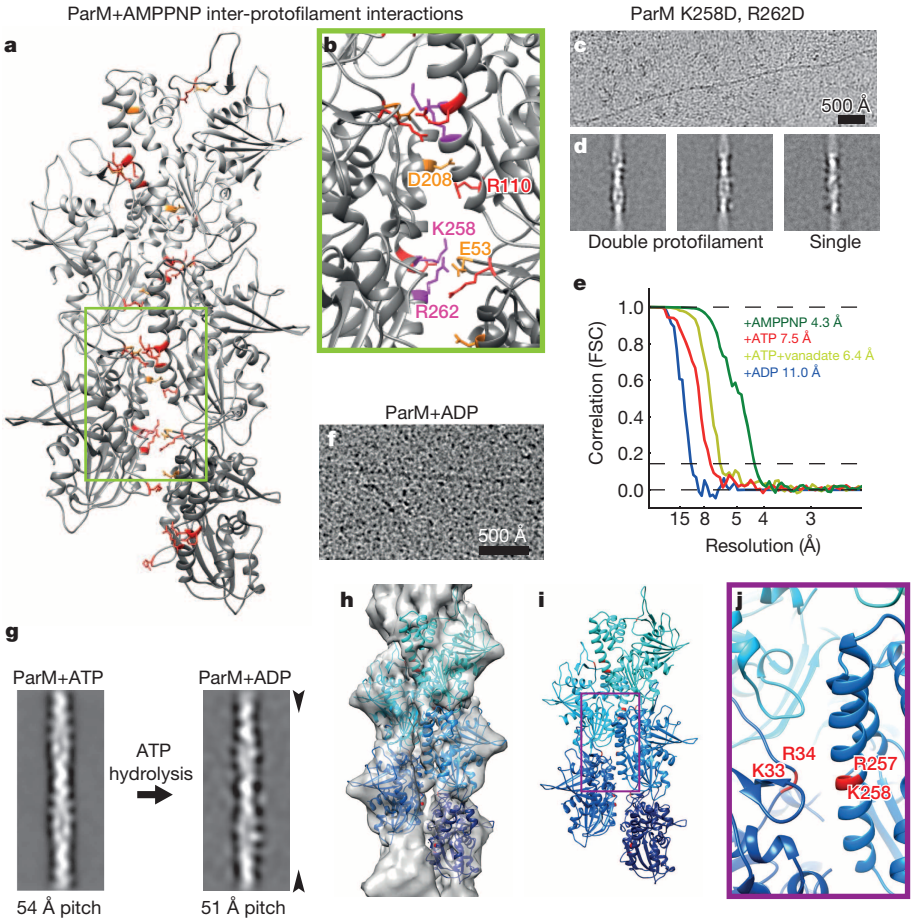

Figure 2 | ParM filaments are made up of two protofilaments held together by salt bridges, which are perturbed when ParM is bound to ADP. **a**, The refined atomic model of ParM+AMPPNP filaments shows that the protofilaments are held together laterally by salt bridges. Basic residues at the interface are highlighted in red and acidic residues in orange (see Extended Data Table 2). Within the protofilaments' longitudinal interfaces, more extensive hydrophobic interactions are observed (see Extended Data Fig. 2). **b**, A magnified view of **a**. The charges of two basic residues at the interface were inverted by mutation for **c** (K258D, R262D). **c**, The resulting protein formed filaments inefficiently. Cryo-EM image showing filaments of ParM(K258D, R262D) assembled with AMPPNP. This experiment was repeated four times. **d**, In addition to normal double-helical filaments, some single-helical filaments were observed by image classification and averaging. **e**, Fourier shell correlation (FSC) curves for the four cryo-EM structures presented in this study (see Extended Data Table 1). **f**, Cryo-EM image of ParM+ADP filaments. High protein concentrations were required to obtain these filaments and monomeric proteins can be seen. This experiment was repeated six times. **g**, Comparison of filtered class averages of ParM+ATP and ParM+ADP filaments. Compared with the ATP bound state, the pitch of the ParM+ADP filaments reduced by ~3 Å (see Supplementary Video 2). **h**, Cryo-EM reconstruction of ParM+ADP filaments at 11 Å resolution with five copies of the ParM+ADP X-ray structure fitted. **i**, The same pseudo-atomic fit without the cryo-EM density. **j**, A magnified view of the perturbed inter-protofilament interface in the ParM+ADP filaments.

(MreB). We propose that small and simple inter-protofilament contacts could have made it possible to change inter-protofilament arrangements relatively easily during evolution since all these actin-like filaments show similar longitudinal contacts[13].

The protofilaments of ParM themselves are held together by an extensive longitudinal contact area (~995 Å^2), containing both hydrophilic and hydrophobic interactions (Extended Data Fig. 2 and Extended Data Table 2). Actin filaments have also been shown to have the same difference in interface size between the longitudinal and lateral contacts[14–16]. Interestingly, this difference has also been observed in tubulin polymers, microtubules[17].

The dynamic instability of ParM is caused by intrinsic ATP hydrolysis in the filament and the resulting ADP-bound filament being less stable[18], while being temporally protected by an ATP cap. We therefore assembled ParM+ATP filaments and obtained a 7.5 Å cryo-EM structure of these filaments (Extended Data Fig. 4). Since the nucleotide state of this structure may be mixed, we devised a way to inhibit the ATPase of ParM with vanadate. Addition of sodium orthovanadate to the ParM+ATP solution retarded filament disassembly and we captured these ParM+ATP+vanadate filaments before complete disassembly and obtained a 6.4 Å structure (Extended Data Fig. 4). Comparison of the three cryo-EM structures (+AMPPNP, +ATP, +ATP+vanadate) indicates that ParM is held in the same rigid, compact conformation, either until ATP is hydrolysed to ADP or until phosphate is released (Extended Data Fig. 4e, f).

Therefore the state with an expected conformational change should be ADP-bound, and since ParM+ADP has a much higher critical concentration for filament formation, we incubated a concentrated solution of ParM with ADP for cryo-EM (Fig. 2f). This specimen yielded a lower resolution reconstruction at 11 Å. Further refinement was not possible, and adding data did not improve the resolution of the structure (Fig. 2e and Extended Data Table 1). This indicated marked flexibility in the ParM+ADP filaments. Surprisingly, the overall helical pitch of the ParM+ADP filaments is smaller than in the other nucleotide states (ADP: 51 Å versus 54 Å; Fig. 2g and Extended Data Table 1). The previously solved ParM+ADP X-ray structure (PDB 1MWM)[6] was subdivided into its two domains and these were fitted as rigid bodies into the ParM+ADP cryo-EM reconstruction (Fig. 2h, i). Since the helical symmetry of ParM+ADP filaments is different from the ParM+ATP filaments, the interaction of ParM

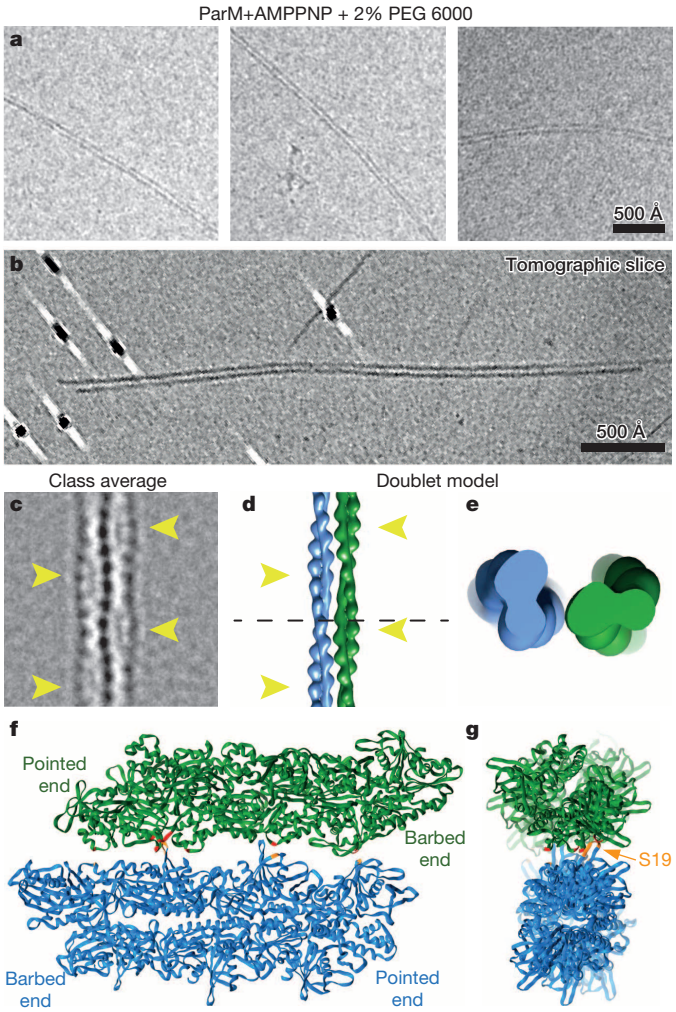

Figure 3 | ParM doublets formed *in vitro*. **a**, Cryo-EM images of ParM doublets formed *in vitro* with crowding agent PEG 6000. This experiment was repeated 15 times. **b**, Slice through an electron cryotomogram (cryo-ET) showing clear lack of super-helicity in the doublets (see Supplementary Video 3). **c**, A two-dimensional class average of the ParM doublet. The thickest parts of double helical ParM filaments have been indicated with yellow arrowheads (see Extended Data Fig. 5). **d**, Model of the doublet, shown in the same orientation as the class average in **c** (see Supplementary Video 4). **e**, An orthogonal, magnified view of the doublet cut at the plane shown as a dashed line in **d**. **f**, Atomic model of the doublet. Residues shown in red in one ParM filament interact with residues in orange in the other filament (see Extended Data Table 2). **g**, An orthogonal view of the doublet, with the filament axes going into the plane of the paper. One of the residues (S19) that forms the doublet interface has been highlighted (see Extended Data Fig. 6).

subunits with each other is also different in the two states. In ParM+ADP filaments, salt bridges at the inter-protofilament interface can no longer be formed and rather repulsing charges are brought close together (Fig. 2j). Additionally, change in helical pitch of the filament may also come with a substantial change in the longitudinal interface. These two factors together could explain why ParM+ADP filaments are less stable, and indicate why ParM filaments rapidly dissociate into monomeric form upon ATP hydrolysis, leading to dynamic instability (Supplementary Video 2).

Having described the structure of the ParM filaments, we then wished to put the structural data in context of the bipolar spindles that segregate plasmid DNA in cells. For bipolar spindles to form, filamentous ParM subunits must engage in another interaction, inter-filament contacts, formed between double-helical filaments. It is known that incubation of ParM filaments with a crowding agent causes them to bundle[19]. However, bundles are not amenable to high-resolution cryo-EM analysis because of their heterogeneity[20]. To obtain a more defined sample, we titrated ParM+AMPPNP with varying amounts of crowding agent. When 2% polyethylene glycol (PEG) 6000 was added to ParM+AMPPNP, we found that ParM filaments dimerized to form 'doublets', containing two double-helical filaments (Fig. 3a and Extended Data Fig. 5a, b). In raw cryo-EM images, doublets appeared as two roughly parallel lines, with no evidence of supercoiling or twisting. Electron cryotomography (cryo-ET) of the doublet specimen confirmed that the filaments do not twist around each other (Fig. 3b and Supplementary Video 3).

We then performed reference-free two-dimensional classification of doublet images (Fig. 3c and Extended Data Fig. 5c). The two ParM filaments in the doublet were perfectly out of phase with each other. When viewed as a projection (in a cryo-EM class average), the thickest part of one filament in the doublet perfectly aligns with the thinnest part of the other double helical filament. We picked small segments along single ParM filaments that formed the doublets and aligned the segments to re-projections of the high-resolution ParM+AMPPNP structure we solved above. Using this alignment, directionality could be assigned to each filament in the doublet. We found that, in 84% of the cases, ParM *in vitro* doublets appeared to be made of two anti-parallel filaments (Extended Data Fig. 5d) while opposite matches were probably due to incorrect assignment of the short segments.

Using the class averages and the directionality assignment, we obtained an averaged model for the ParM doublet (Fig. 3d–g, Extended Data Fig. 5e, f and Supplementary Video 4). Two ParM monomers from adjoining filaments in the doublet model were found to be in a similar orientation as observed in a previous crystal structure of ParM (Extended Data Fig. 6a, b)[3]. The model of the doublet predicts residues in ParM that should be important in doublet formation (Fig. 3f, g and Extended Data Table 2) and confirmed earlier work, including mutations that modulate the strength of the inter-filament contact. One such set of mutations consisted of S19R and G21R[3]. These mutations had been selected previously because they are located the furthest away from the filament axis, essentially sticking out, but are shown here directly to be involved in the inter-filament contact. In line with this, mutant ParM(S19R, G21R) spontaneously formed doublets and bundles (Extended Data Fig. 6c), without any crowding agent present in solution, validating both the previous total internal reflection fluorescence data[3] as well as the current atomic model of the ParM doublet.

Previous imaging by total internal reflection fluorescence microscopy of the reconstituted ParMRC spindles[3] as well as the model of the ParM doublet derived here are *in vitro* experiments. To test whether the doublets have physiological relevance, we visualized ParM filaments inside growing *E. coli* cells. Previously, direct observation of ParM filaments by cryo-EM was only possible by cryo-sectioning of frozen bacterial cells since whole cells were deemed too thick[19]. Importantly, in vitreous sections filaments could only be visualized end-on, not revealing much about the inter-filament contacts. Using new direct electron detectors, signal-to-noise has been dramatically improved, so we aimed at imaging bipolar spindles directly inside cells using whole-cell cryo-ET.

As a first test, we overexpressed a mutant of ParM (D170A) that hydrolysed ATP much more slowly in thin *E. coli* cells. As observed previously in vitreous sections[19], cryo-ET of these cells (Fig. 4a) allowed unambiguous identification of the overexpressed ParM mutant protein through its tendency to form extremely large bundles.

We then used plasmids with different copy numbers[21], all of which contained the entire ParMRC locus and transformed them in turn into *E. coli* cells. Cryo-ET of these cells revealed the presence of doublets in all cases (Fig. 4b–d, Supplementary Videos 5 and 6, Extended Data Fig. 7 and Extended Data Table 3). All doublets were roughly aligned with the long cell axis, and were never observed perpendicular to the cell axis. Although bundles were observed in

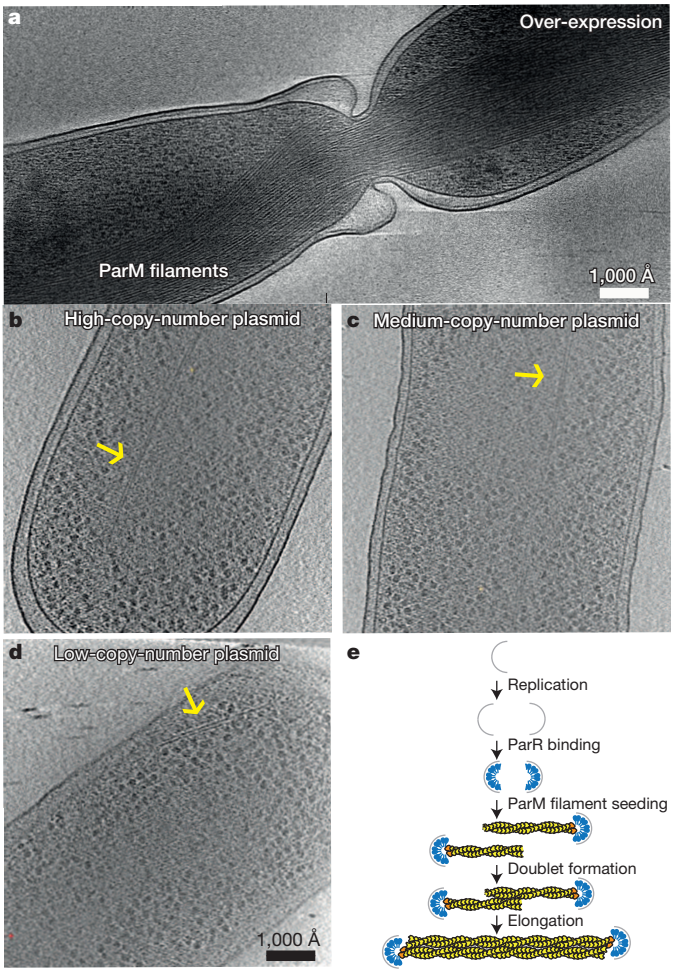

Figure 4 | ParM doublets in *E. coli* cells, imaged by cryo-ET. **a**, A mutant of ParM that hydrolyses ATP more slowly (D170A) was overexpressed in *E. coli* cells. Tomographic slices show large bundles of ParM blocking cell division. This experiment was performed two times. **b**, The ParMRC operon driven from high-copy-number plasmid pDD19. Tomographic slice showing an example of observed doublets. **c**, Tomographic slice for a medium-copy-number plasmid (pKG321). **d**, Tomographic slice for a low-copy-number plasmid, emulating the native low-copy-number R1 plasmids (pKG491, 'mini-R1' replicon) in *E. coli* (see Supplementary Videos 5 and 6 to view entire tomograms). Each experiment with different copy-number plasmids was performed once. **e**, Schematic depicting proposed asynchronous plasmid DNA segregation. Bipolar ParM spindles are seeded when replication has produced two *parC* centromeric regions, still in close proximity. Each seeds one unipolar ParM filament, which then come together in an antiparallel fashion to form the segregating bipolar spindle. Non-productive unipolar filaments or spindles that lack plasmid attachment will be destroyed through the dynamic instability of ParM. This is in contrast to earlier ideas in which all sister plasmids would be segregated through one bundle of filaments, containing double the number of unipolar filaments as the copy number of the plasmid in the cell[19].

the high- and medium-copy-number plasmid cases, they were not observed in the low-copy-number (mini-R1) case, where partitioning via ParMRC is required for plasmid stability[22]. These cryo-ET data are in line with previous immuno-light microscopy data, where single pole-to-pole filaments were only observed in 40% of cells[1,10] and the other cells showed several localized clusters or more complex patterns.

The above data showed that ParM doublets are found in cells containing the ParMRC locus, and are probably the machinery that actively segregates plasmid DNA to opposite ends of the dividing cell, even though antiparallel arrangement of ParM filaments in cellular doublets can only be inferred from the *in vitro* studies above. It is interesting to observe that the ratios of doublets observed per cell were the same as the ratios of the expected copy numbers of the three plasmids, although it needs to be noted that numbers remain small because of the low-throughput nature of cryo-ET (Extended Data Table 3). The ratios might indicate that each doublet carries a defined payload of DNA cargo, a fixed number of plasmids containing the *parC* locus. We propose that ParMRC spindles consisting solely of doublets elegantly circumvent the problem of synchronizing plasmid replication, filament attachment and bundle formation for all plasmids in the cell: each pair of plasmid sisters is segregated by their own spindle. The resulting asynchronous plasmid segregation is schematically summarized in Fig. 4e. Indeed, it is known that R1 plasmids are replicated randomly throughout the cell cycle[23,24]. In contrast, eukaryotic DNA segregation requires cohesion, kinetochore checkpoints and other dedicated machinery since all material is segregated with one coordinated and synchronized spindle.

Online Content Methods, along with any additional Extended Data display items and Source Data, are available in the online version of the paper; references unique to these sections appear only in the online paper.

Received 14 November 2014; accepted 2 March 2015.
Published online 27 April 2015.

1. Møller-Jensen, J., Jensen, R. B., Löwe, J. & Gerdes, K. Prokaryotic DNA segregation by an actin-like filament. *EMBO J.* **21,** 3119–3127 (2002).
2. Gerdes, K., Howard, M. & Szardenings, F. Pushing and pulling in prokaryotic DNA segregation. *Cell* **141,** 927–942 (2010).
3. Gayathri, P. *et al.* A bipolar spindle of antiparallel ParM filaments drives bacterial plasmid segregation. *Science* **338,** 1334–1337 (2012).
4. Orlova, A. *et al.* The structure of bacterial ParM filaments. *Nature Struct. Mol. Biol.* **14,** 921–926 (2007).
5. Popp, D. *et al.* Molecular structure of the ParM polymer and the mechanism leading to its nucleotide-driven dynamic instability. *EMBO J.* **27,** 570–579 (2008).
6. van den Ent, F., Møller-Jensen, J., Amos, L. A., Gerdes, K. & Löwe, J. F-actin-like filaments formed by plasmid segregation protein ParM. *EMBO J.* **21,** 6935–6943 (2002).
7. Møller-Jensen, J., Ringgaard, S., Mercogliano, C. P., Gerdes, K. & Löwe, J. Structural analysis of the ParR/parC plasmid partition complex. *EMBO J.* **26,** 4413–4422 (2007).
8. Schumacher, M. A. *et al.* Segrosome structure revealed by a complex of ParR with centromere DNA. *Nature* **450,** 1268–1271 (2007).
9. Garner, E. C., Campbell, C. S., Weibel, D. B. & Mullins, R. D. Reconstitution of DNA segregation driven by assembly of a prokaryotic actin homolog. *Science* **315,** 1270–1274 (2007).
10. Møller-Jensen, J. *et al.* Bacterial mitosis: ParM of plasmid R1 moves plasmid DNA by an actin-like insertional polymerization mechanism. *Mol. Cell* **12,** 1477–1487 (2003).
11. Izoré, T., Duman, R., Kureisaite-Ciziene, D. & Löwe, J. Crenactin from *Pyrobaculum calidifontis* is closely related to actin in structure and forms steep helical filaments. *FEBS Lett.* **588,** 776–782 (2014).
12. Ozyamak, E., Kollman, J., Agard, D. A. & Komeili, A. The bacterial actin MamK: *in vitro* assembly behavior and filament architecture. *J. Biol. Chem.* **288,** 4265–4277 (2013).
13. Ozyamak, E., Kollman, J. M. & Komeili, A. Bacterial actins and their diversity. *Biochemistry* **52,** 6928–6939 (2013).
14. Fujii, T., Iwane, A. H., Yanagida, T. & Namba, K. Direct visualization of secondary structures of F-actin by electron cryomicroscopy. *Nature* **467,** 724–728 (2010).
15. von der Ecken, J. *et al.* Structure of the F-actin–tropomyosin complex. *Nature* **519,** 114–117 (2015).
16. Galkin, V. E., Orlova, A., Vos, M. R., Schröder, G. F. & Egelman, E. H. Near-atomic resolution for one state of F-actin. *Structure* **23,** 173–182 (2015).
17. Alushin, G. M. *et al.* High-resolution microtubule structures reveal the structural transitions in αβ-tubulin upon GTP hydrolysis. *Cell* **157,** 1117–1129 (2014).
18. Garner, E. C., Campbell, C. S. & Mullins, R. D. Dynamic instability in a DNA-segregating prokaryotic actin homolog. *Science* **306,** 1021–1025 (2004).
19. Salje, J., Zuber, B. & Löwe, J. Electron cryomicroscopy of *E. coli* reveals filament bundles involved in plasmid DNA segregation. *Science* **323,** 509–512 (2009).
20. Popp, D., Narita, A., Iwasa, M., Maéda, Y. & Robinson, R. C. Molecular mechanism of bundle formation by the bacterial actin ParM. *Biochem. Biophys. Res. Commun.* **391,** 1598–1603 (2010).
21. Dam, M. & Gerdes, K. Partitioning of plasmid R1. Ten direct repeats flanking the *parA* promoter constitute a centromere-like partition site *parC*, that expresses incompatibility. *J. Mol. Biol.* **236,** 1289–1298 (1994).
22. Breuner, A., Jensen, R. B., Dam, M., Pedersen, S. & Gerdes, K. The centromere-like *parC* locus of plasmid R1. *Mol. Microbiol.* **20,** 581–592 (1996).
23. Gustafsson, P. & Nordström, K. Control of plasmid R1 replication: kinetics of replication in shifts between different copy number levels. *J. Bacteriol.* **141,** 106–110 (1980).

24. Nordström, K. Plasmid R1–replication and its control. *Plasmid* **55,** 1–26 (2006).

Supplementary Information is available in the online version of the paper.

Acknowledgements We thank F. van den Ent, K. Gerdes and P. Gayathri for help with sample preparation, and C. Johnson, C. Savva and F. de Haas for help with data collection. This work was supported by the Medical Research Council (U105184326) and the Wellcome Trust (095514/Z/11/Z). T.A.M.B. is the recipient of Federation of European Biochemical Societies (FEBS) and European Molecular Biology Organization (EMBO) (ALTF 3-2013) long-term fellowships. G.N.M. was funded by Medical Research Council grant MC-UP-A025-1012.

Author Contributions T.A.M.B. and J.L. designed experiments; T.A.M.B. performed experiments; T.A.M.B., G.N.M., C.S. and J.L. analysed data; T.A.M.B. and J.L. wrote the paper.

Author Information Cryo-EM and cryo-ET data have been deposited in the Electron Microscopy Data Bank under accession codes EMD-2848, EMD-2849 and EMD-2850. Atomic coordinates of the ParM+AMPPNP filament structure and the ParM antiparallel doublet model have been deposited in the Protein Data Bank under accession codes 5AEY and 5AI7. Reprints and permissions information is available at www.nature.com/reprints. The authors declare no competing financial interests. Readers are welcome to comment on the online version of the paper. Correspondence and requests for materials should be addressed to J.L. (jyl@mrc-lmb.cam.ac.uk).

METHODS

No statistical methods were used to predetermine sample size.

Protein expression and purification. ParM (UniProt: PARM_ECOLX) and ParM mutants were expressed from plasmid *pJSC1* and its derivatives[25] in *E. coli* BL21-AI cells and purified as described previously[3,25]. Buffer MR was used in all experiments: 50 mM Tris-HCl, 100 mM KCl, and 1 mM $MgCl_2$, pH 7.0.

Wild-type ParM and ParM(S19R, G21R). ParM was purified by ammonium sulphate precipitation (at a final concentration of 10% (sat.) ammonium sulphate) of the lysate, followed by addition of ATP to the re-suspended pellet. ParM filaments were pelleted by centrifugation at 100,000*g*, and the resulting pellet containing pure protein was re-suspended in buffer and further purified by size exclusion chromatography on a Sephacryl S-200 column (GE Healthcare).

ParM(K258D, R262D). The protein was purified using a 5 ml HiTrap Q HP column (GE Healthcare), and eluted at increasing KCl concentrations. Fractions containing ParM were pooled and further purified by size exclusion on a Sephacryl S-200 column (GE Healthcare) into buffer MR. Concentrated aliquots of pure protein were frozen and stored at −80 °C until further investigation.

Sample preparation for microscopy. ParM+AMPPNP and ParM+ATP. ParM protein (10 μM) was incubated with 2 mM nucleotide in a total volume of 100 μl for 5 min at room temperature (22 °C) before cryo-EM sample preparation. The same procedure was used for polymerization of the ParM S19R, G21R mutant.

ParM+ATP+vanadate and ParM+ADP+vanadate. ParM protein (10 μM) was incubated with 2 mM ATP or ADP and 4 mM sodium orthovanadate in a total volume of 100 μl for 2 h or 5 min at room temperature before cryo-EM sample preparation.

ParM+ADP. 400 μM ParM was incubated with 10 mM ADP in a total volume of 25 μl for 5 min at room temperature.

ParM(K258D, R262D)+AMPPNP. Protein (60 μM) was incubated with 2 mM AMPPNP in a total volume of 100 μl for 5 min at room temperature.

ParM *in vitro* doublets. ParM protein (20 μM) was incubated with 2 mM AMPPNP in the presence of 2% (w/v) PEG 6000 in a 100 μl for 5 min at room temperature.

ParM(D170A)-overexpressing cells. ParM was expressed to high levels for cryo-ET using the plasmid pRBJ212 (ParM(D170A), *ptac* promoter)[1] transformed into *E. coli* B/R266 cells. Cells were grown in M9 medium at 30 °C and induced with 1 mM IPTG at an attenuance $D_{600\,nm} \approx 0.5$. Samples were prepared 4 h after induction.

Bacterial cells with different copy-number plasmids containing the ParMRC locus. *E. coli* strain B/R266 (ref. 26) was transformed with high- (pDD19), medium- (pKG321) or low-copy (pKG491) plasmids and grown in M9 medium supplemented with 100 μg ml^{-1} ampicillin at 30 °C (ref. 21). Cells were grown to $D_{600\,nm} \approx 0.4–0.6$ (grown to logarithmic growth phase) before sample preparation for cryo-EM.

Cryo-EM grid preparation. Samples for cryo-EM were prepared by pipetting 2.5 μl of the sample onto a freshly glow-discharged Quantifoil Cu/Rh 200 mesh grids (R2/2 for purified protein, and R3.5/1 for cellular tomography) and plunge frozen into liquid ethane in a Vitrobot Mark IV (FEI). Only for cryo-ET, 11 μl of sample were pre-mixed with 1 μl of protein-A conjugated with 10 nm colloidal gold (Cell Microscopy Center, Utrecht University, The Netherlands). Plunged grids were transferred to liquid nitrogen and stored.

Electron microscopy data collection. Two-dimensional cryo-EM data were collected using either an FEI Krios microscope operated at 300 kV or a FEI Spirit microscope operated at 120 kV. High-throughput data were collected on the FEI Krios using EPU software at an unbinned calibrated pixel size of 1.30 Å or 1.07 Å on a Falcon II direct electron detector. A combined total dose of 25–32 electrons per square ångström was applied with each exposure that lasted 1 s. Images were collected at 1–6 μm underfocus. Tilt series data were collected on an FEI Krios equipped with a Quantum energy filter (Gatan) using SerialEM software[27], on a K2 direct electron detector operating in counting mode. Tilt series data were typically collected from ±60° with 1° tilt increment at 4–12 μm underfocus with a combined dose of about 120 electrons per square ångström applied over the entire series.

Image processing and data analysis. Real-space helical reconstruction. An averaged power spectrum for each cryo-EM image was calculated using CTFFIND[28], and images showing clear Thon rings were retained. ParM filaments were extracted from the selected images using SPRING and EMAN2[29,30]. The helical symmetry of each sample was accurately determined by comparing the power spectrum of the aligned segments with power spectra of re-projections of the calculated reconstructions. Experimentally determined helical parameters (Extended Data Table 1) were used for refinement using the program segmentrefine3D in SPRING. The final volumes were compensated for the B-factor and filtered to the obtained resolutions (Extended Data Table 1). Resolution of the structure was estimated using gold-standard Fourier shell correlation measurements in SPRING and additionally using ResMap[31]. Visualization of densities was performed in UCSF Chimera[32].

Atomic model building. The atomic structure from PDB 4A62 (ref. 3) was fitted into the cryo-EM density of ParM+AMPPNP using MolRep[33]. Maximum-likelihood refinement of the atomic structure against the cryo-EM density was performed in REFMAC5 (ref. 34) using standard protein stereochemistry and additional external restraints based on PDB 4A62, generated in ProSMART[35]. Model building was performed in COOT and MAIN[36,37].

Rigid body fitting. ParM was divided into two sub-domains, based on the previous ParM+ADP X-ray structure (PDB 1MWM). Each sub-domain was declared as a rigid body and these were fitted into the ParM+ADP filament structure using REFMAC5.

Polarity assignment of ParM filaments in doublets. First, images of ParM doublets were carefully selected on the basis of image quality (as assessed by a visual inspection of power spectra), and by a visual assessment of the distance between the two filaments in the doublet. The assumption made from the appearance of the class averages was that images in which the distance between the centres of two ParM filaments in the doublet was maximum would show ParM filaments entirely in the same *x*–*y* plane (the *z*-axis being the path of the electron beam in the microscope). The two ParM filaments in all the doublets in these selected images were picked manually using EMAN2 (ref. 30). The manual pick was used to extract short segments along each filament in the doublet. The extracted segments were aligned to re-projections of the high-resolution ParM+AMPPNP filament model using SPRING[29]. In five out of the six doublets analysed, the assigned directionality of ParM filaments was predominantly anti-parallel and in one case the assignment was mostly parallel.

Derivation of the doublet model. The ParM doublet is not a true helical specimen, thus conventional helical reconstruction could not be performed. This difficulty of characterizing higher-order filament structures of ParM filaments has been previously reported[20]. The average distance between the centres of the two ParM filaments in the doublet was found to be 65.1 Å by analysis of one-dimensional line-profiles of all obtained class averages. Two copies of the high-resolution cryo-EM structure of the ParM+AMPPNP filaments were accordingly placed with their centres 65.1 Å apart in space in an anti-parallel orientation. The placement was repeated for all possible combinations of the azimuthal angles of both filaments. Re-projections of all these resulting volumes were aligned with all obtained class averages. As expected intuitively from an inspection of the class averages, models in which the thickest part of one ParM filament overlapped with the thinnest part of the other filament in the doublet had higher cross-correlation scores. We placed two copies of the atomic structure of the ParM+AMPPNP in the volume with the highest score. Since this was not a standard cryo-EM reconstruction, meaning resulting atomic accuracy would be somewhat lower, we only used the Cα atoms for determining distances shown in Extended Data Table 2.

Tomographic reconstructions. Tilt series data were aligned using IMOD[38] and three-dimensional reconstructions were conducted using the SIRT algorithm implemented in Tomo3D[39]. Visualization of data was done using IMOD and UCSF Chimera[32].

25. Salje, J. & Löwe, J. Bacterial actin: architecture of the ParMRC plasmid DNA partitioning complex. *EMBO J.* **27,** 2230–2238 (2008).
26. Cooper, S. & Helmstetter, C. E. Chromosome replication and the division cycle of *Escherichia coli* B/r. *J. Mol. Biol.* **31,** 519–540 (1968).
27. Mastronarde, D. N. Automated electron microscope tomography using robust prediction of specimen movements. *J. Struct. Biol.* **152,** 36–51 (2005).
28. Mindell, J. A. & Grigorieff, N. Accurate determination of local defocus and specimen tilt in electron microscopy. *J. Struct. Biol.* **142,** 334–347 (2003).
29. Desfosses, A., Ciuffa, R., Gutsche, I. & Sachse, C. SPRING – an image processing package for single-particle based helical reconstruction from electron cryomicrographs. *J. Struct. Biol.* **185,** 15–26 (2014).
30. Tang, G. *et al.* EMAN2: an extensible image processing suite for electron microscopy. *J. Struct. Biol.* **157,** 38–46 (2007).
31. Kucukelbir, A., Sigworth, F. J. & Tagare, H. D. Quantifying the local resolution of cryo-EM density maps. *Nature Methods* **11,** 63–65 (2014).
32. Pettersen, E. F. *et al.* UCSF Chimera–a visualization system for exploratory research and analysis. *J. Comput. Chem.* **25,** 1605–1612 (2004).
33. Vagin, A. & Teplyakov, A. Molecular replacement with MOLREP. *Acta Crystallogr. D* **66,** 22–25 (2010).
34. Murshudov, G. N. *et al.* REFMAC5 for the refinement of macromolecular crystal structures. *Acta Crystallogr. D* **67,** 355–367 (2011).
35. Nicholls, R. A., Fischer, M., McNicholas, S. & Murshudov, G. N. Conformation-independent structural comparison of macromolecules with ProSMART. *Acta Crystallogr. D* **70,** 2487–2499 (2014).
36. Emsley, P. & Cowtan, K. Coot: model-building tools for molecular graphics. *Acta Crystallogr. D* **60,** 2126–2132 (2004).
37. Turk, D. MAIN software for density averaging, model building, structure refinement and validation. *Acta Crystallogr. D* **69,** 1342–1357 (2013).
38. Kremer, J. R., Mastronarde, D. N. & McIntosh, J. R. Computer visualization of three-dimensional image data using IMOD. *J. Struct. Biol.* **116,** 71–76 (1996).
39. Agulleiro, J. I. & Fernandez, J. J. Fast tomographic reconstruction on multicore computers. *Bioinformatics* **27,** 582–583 (2011).

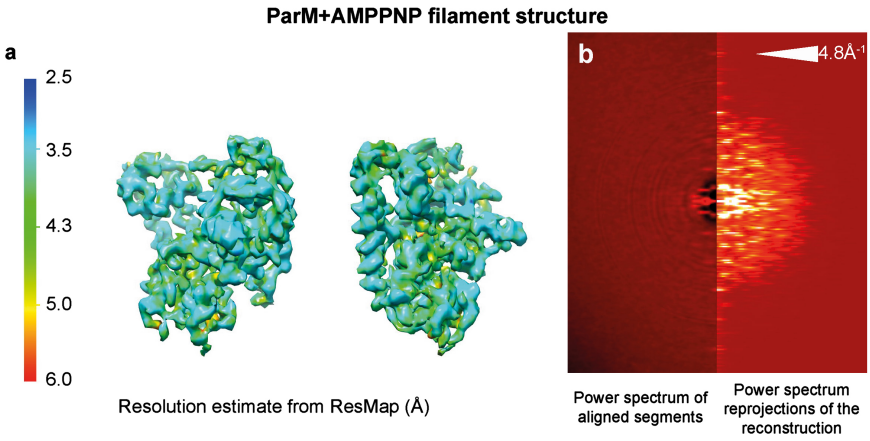

Extended Data Figure 1 | Resolution estimate of the ParM+AMPPNP reconstruction. **a**, Resolution of the ParM+AMPPNP reconstruction was estimated using ResMap and this estimate was plotted back onto the cryo-EM density. Blue indicates high resolution; red indicates lower resolution. **b**, The power spectrum of the aligned segments (left) compared with the power spectrum of the re-projection of the cryo-EM reconstruction (right). A reflection is observed in both cases at 4.8 $Å^{-1}$, indicating that the resolution extends beyond this shell. See Fig. 2e for Fourier shell correlation curves.

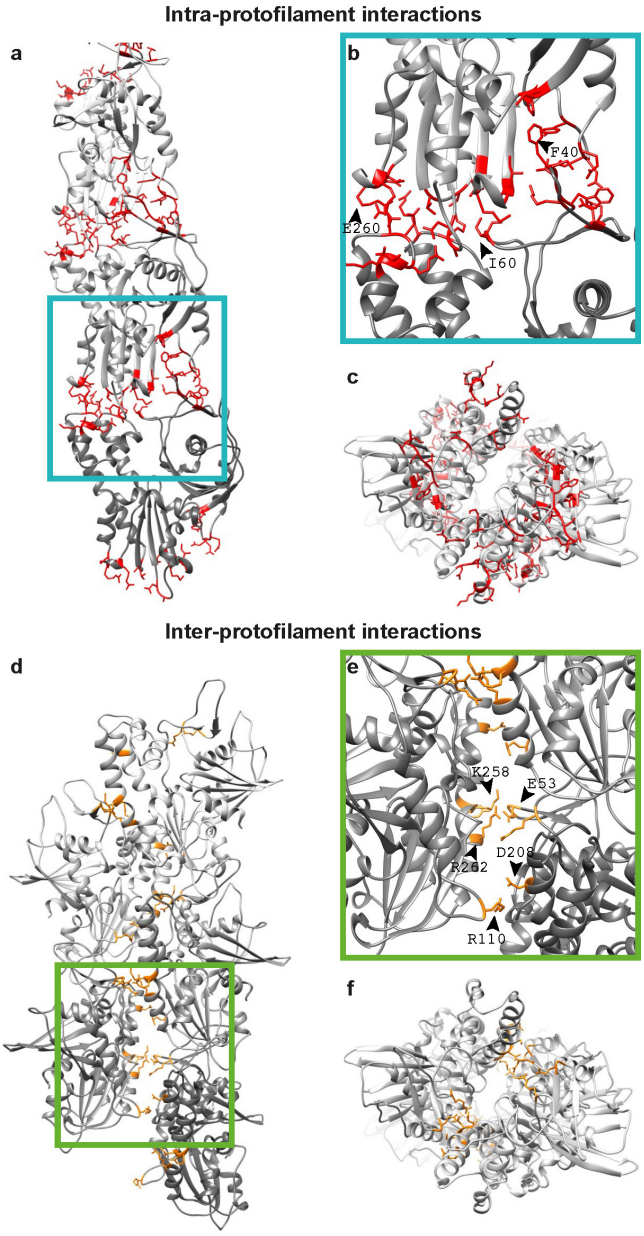

Extended Data Figure 2 | Intra- and inter-protofilament interactions in ParM filaments. **a**, Atomic model of one protofilament (strand) of ParM is shown with the residues at the protein–protein interface highlighted in red. See Extended Data Table 2 for a detailed list. **b**, A magnified view of the interface. Three residues at the interface have been labelled. **c**, The complete ParM filament (that is, both protofilaments/strands) shown end-on. **d**, Atomic model of the ParM filament with the inter-protofilament residues at the protein–protein interface highlighted in orange. **e**, A magnified view of **d**. Salt bridging residues are labelled. **f**, An orthogonal view of **d**. See Extended Data Table 2 for a detailed list of interacting residues.

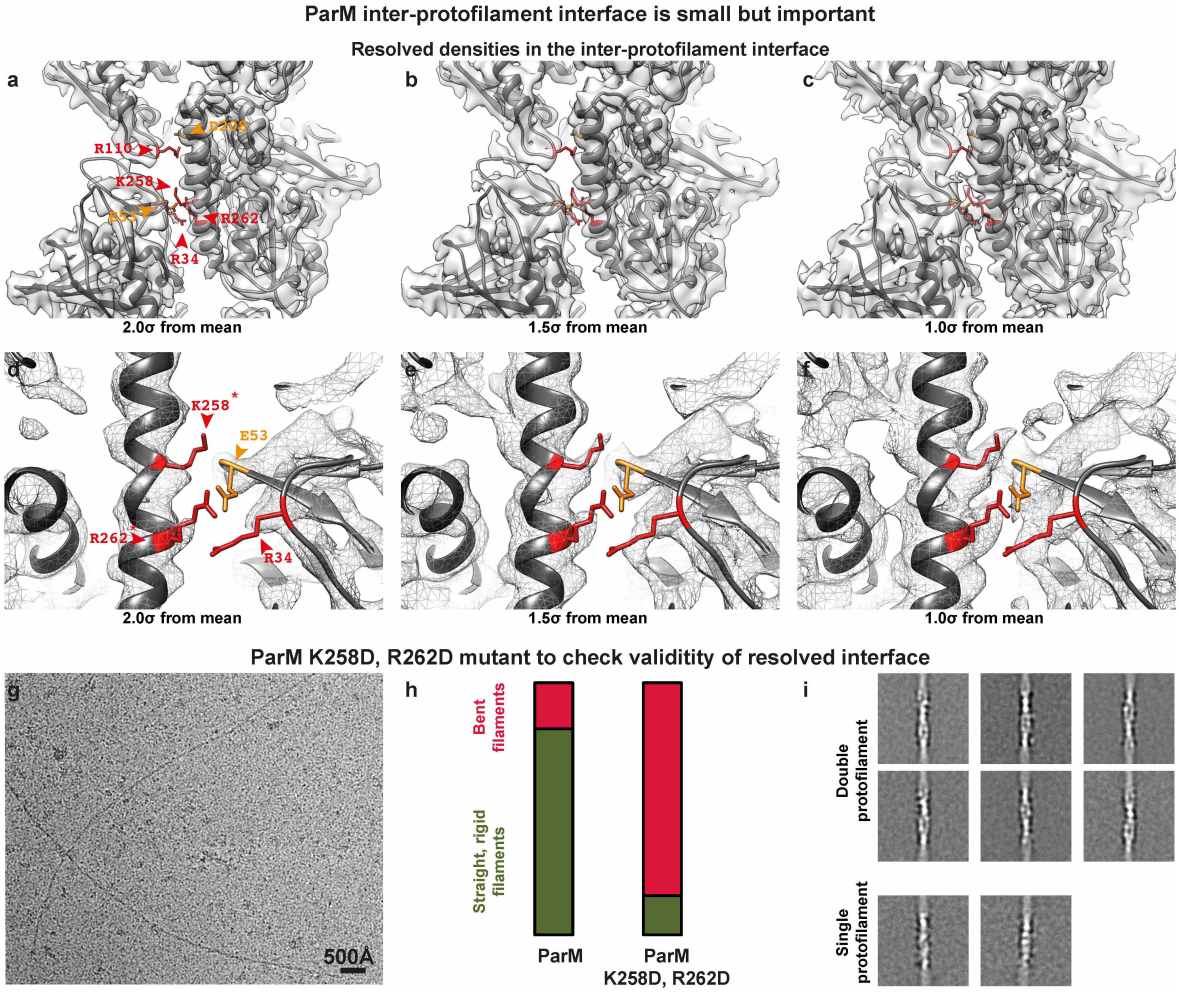

Extended Data Figure 3 | The ParM inter-protofilament interface is small but important. **a**, Cryo-EM density for the ParM+AMPPNP filament is shown at an isosurface contour level of 2.0σ from the mean value. Overlaid on the density, refined atomic coordinates from REFMAC are additionally displayed as grey ribbons. Residues forming salt bridges at the inter-protofilament interface are highlighted. **b**, The same figure as **a**, except the cryo-EM density shown at an isosurface contour level of 1.5σ from the mean; **c**, 1.0σ from the mean. **d**–**f**, A magnified view of the primary salt-bridged interface consisting of charged residues that form the ParM inter-protofilament interface. The cryo-EM density is shown as a mesh at three different contour levels to demonstrate resolved side-chain densities. Positively charged residues are highlighted in red; negatively charged residues are highlighted in orange. **g**, Two residues (K258 and R262) that were the best resolved (marked with an asterisk in **d**), were mutated to aspartic acid to test the importance of this inter-protofilament interface. A cryo-EM image of this mutant protein assembled with AMPPNP is shown. A much higher concentration of the protein was required to obtain filaments on cryo-EM grids (Methods). This experiment was repeated four times. **h**, Randomly selected cryo-EM images of ParM+AMPPNP and ParM(K258D, R262D)+AMPPNP were used to count occurrences of straight and bent filaments by visual inspection. The results of this quantification are shown as a percentage bar diagram. For the ParM protein, 82% of all filaments were classified as straight, while 18% were bent ($n = 345$). Using exactly the same classification criteria, only 15% of the filaments were found to be straight and 85% of the filaments were bent ($n = 45$) for the ParM(K258D, R262D) mutant protein. **i**, Reference-free class averages show that most of the ParM(K258D, R262D) filaments are made up of double protofilaments like wild-type ParM. Some class averages show evidence of bending. A few class averages show that single protofilaments were present in the sample (lower panels). However, the double mutation destabilizes the entire ParM filament, making filament formation an unfavourable reaction, illustrating that even though the inter-protofilament interface is small, it is critical for ParM filament formation.

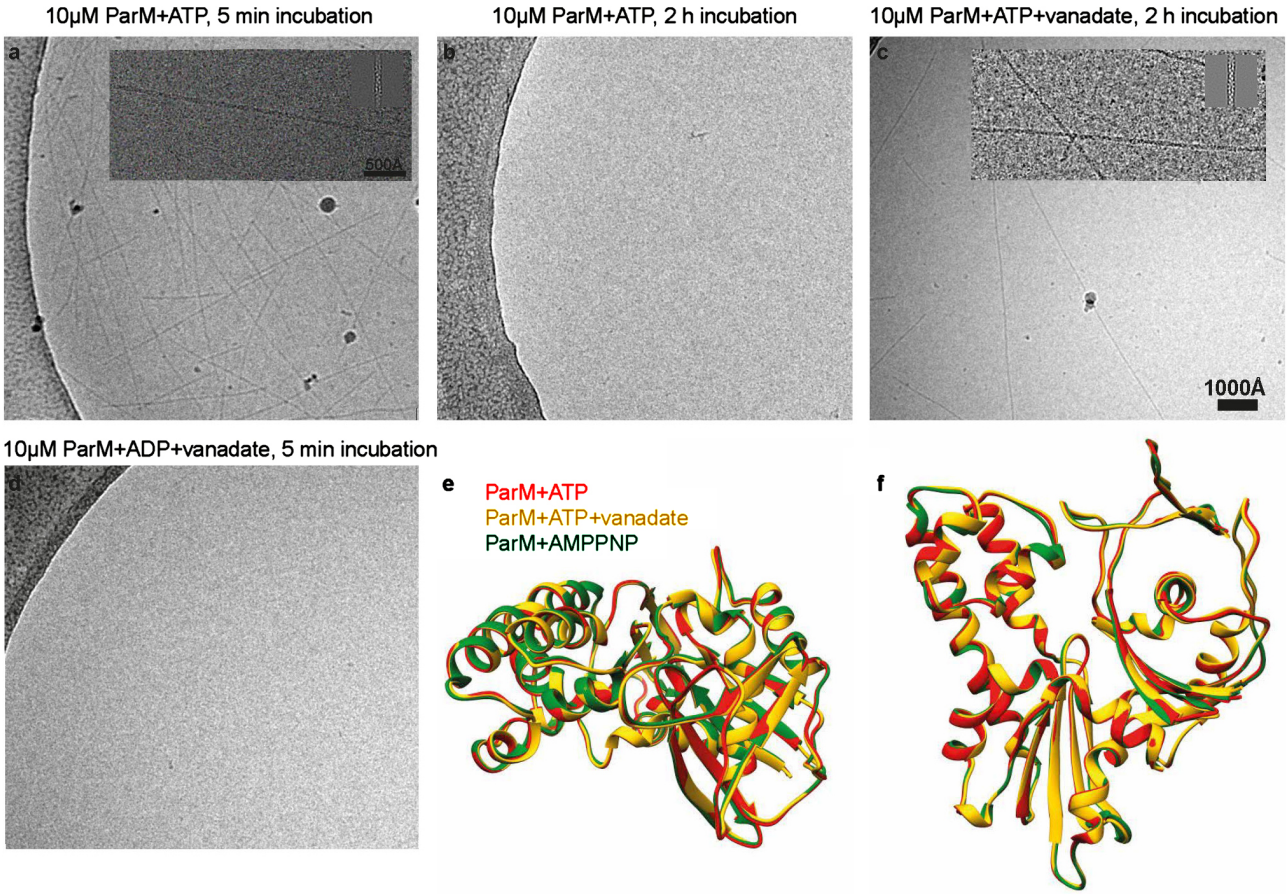

Extended Data Figure 4 | ParM adopts a compact conformation until ATP is hydrolysed to ADP or until phosphate is released. **a**, ParM protein (10 μM) was incubated with ATP (2 mM) and cryo-EM samples were prepared after 5 min. Many filaments were observed on the grid. This experiment was repeated ten times. **b**, After 2 h, no filaments were seen in the same reaction. Presumably, ATP had been hydrolysed and ParM had returned to monomeric form. This experiment was repeated three times. **c**, When sodium orthovanadate (4 mM) was included in the reaction, filaments could be observed, even after 2 h. This experiment was repeated three times. **d**, The same reaction as **a**, except ATP was replaced by ADP. No filaments were observed in this reaction. This experiment was repeated four times. **e**, **f**, We performed real-space helical reconstruction of the ParM+ATP filaments (red) and ParM+ATP+vanadate filaments (yellow), and compared them with the ParM+AMPPNP filament structure (green). Comparison shows that ParM is held in a very similar conformation until hydrolysis of ATP is complete or until phosphate is released since we currently cannot distinguish these two possible effects of vanadate. See Fig. 2e for resolution estimates and Extended Data Table 1 for image-processing statistics.

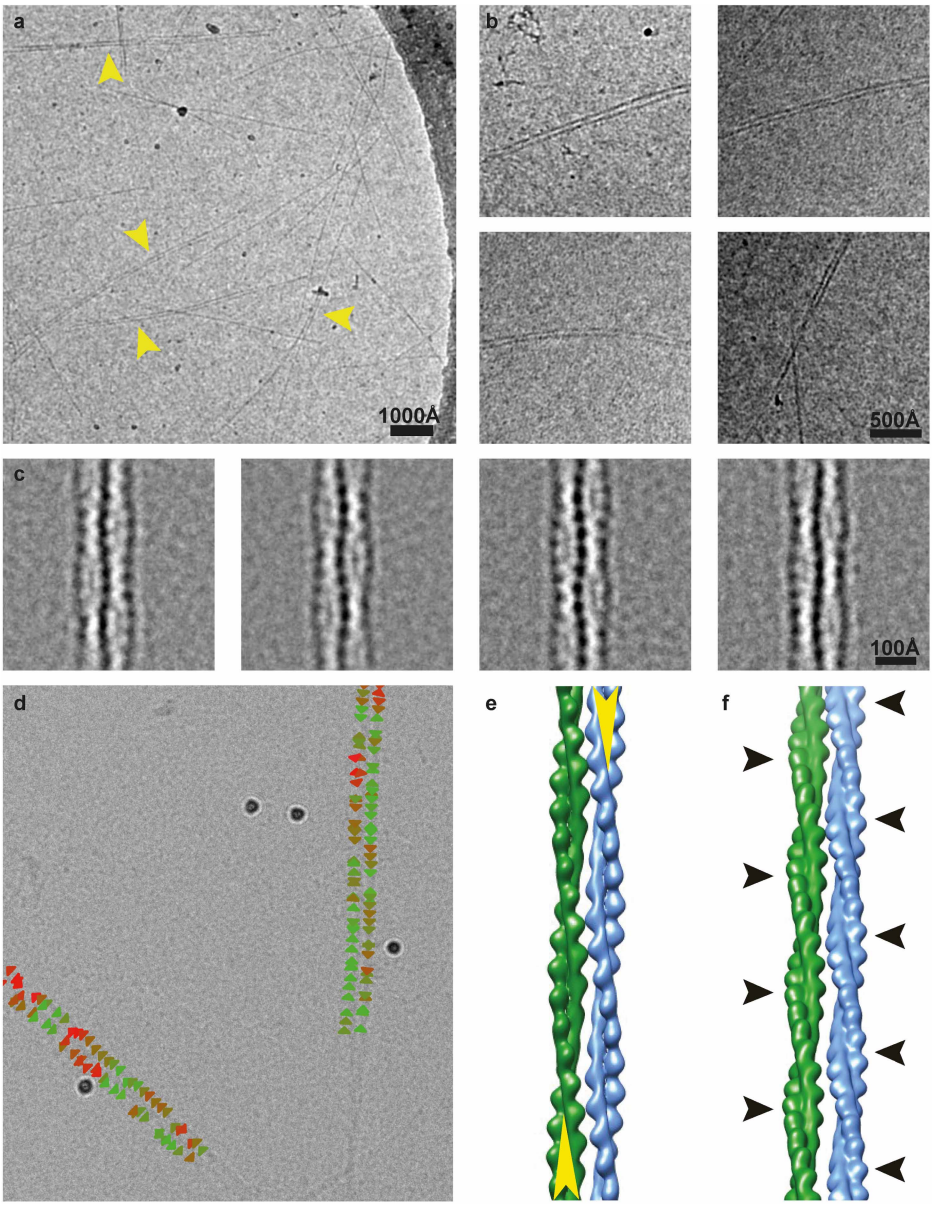

Extended Data Figure 5 | Model of the ParM doublet. **a**, A cryo-EM image of ParM+AMPPNP + 2% PEG 6000. Instances of doublets are marked with yellow arrowheads. This experiment was repeated 15 times. **b**, More examples of ParM doublets observed in cryo-EM. **c**, Class averages of the doublets. **d**, Directionality assignment of the filaments in the doublet. Individual sub-segments and their assigned directionality are indicated by triangles, coloured on the basis of the cross-correlation score in the alignment procedure: red indicates a poor cross correlation score; green indicates a good score. **e**, A schematic model of the anti-parallel ParM doublet. Directionality is indicated with a yellow arrow. **f**, The thickest parts of ParM filaments of the doublet (as they appear in projection) are marked with black arrowheads.

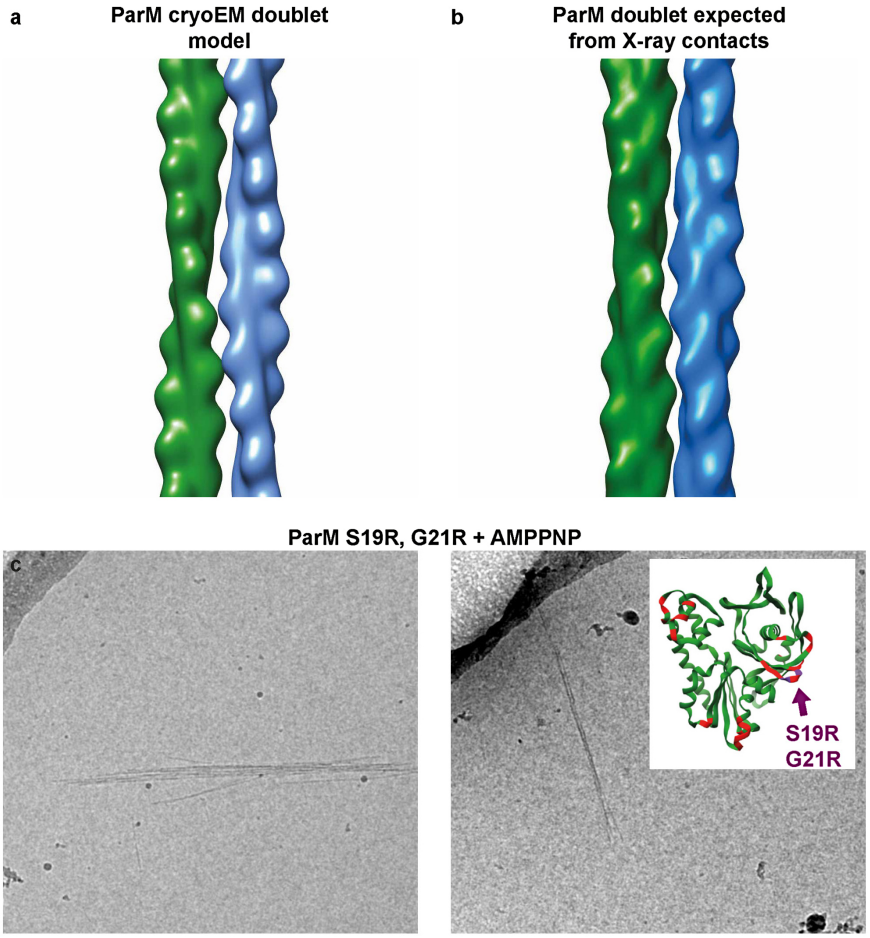

Extended Data Figure 6 | Validation of the doublet model. **a**, Two ParM filaments arranged in an anti-parallel orientation, as obtained from the ParM cryo-EM doublet model. **b**, Two ParM filaments arranged in an anti-parallel orientation, obtained from crystal packing of a monomeric ParM X-ray structure (PDB 4A62)[3]. **c**, Two residues at the interface of the doublet (see Extended Data Table 2), S19 and G21, were mutated to arginine to improve affinity of ParM filaments to each other. Cryo-EM images of the mutant protein with AMPPNP show spontaneous doublet formation and filament bundling without crowding agent, validating the doublet model. This experiment was repeated six times.

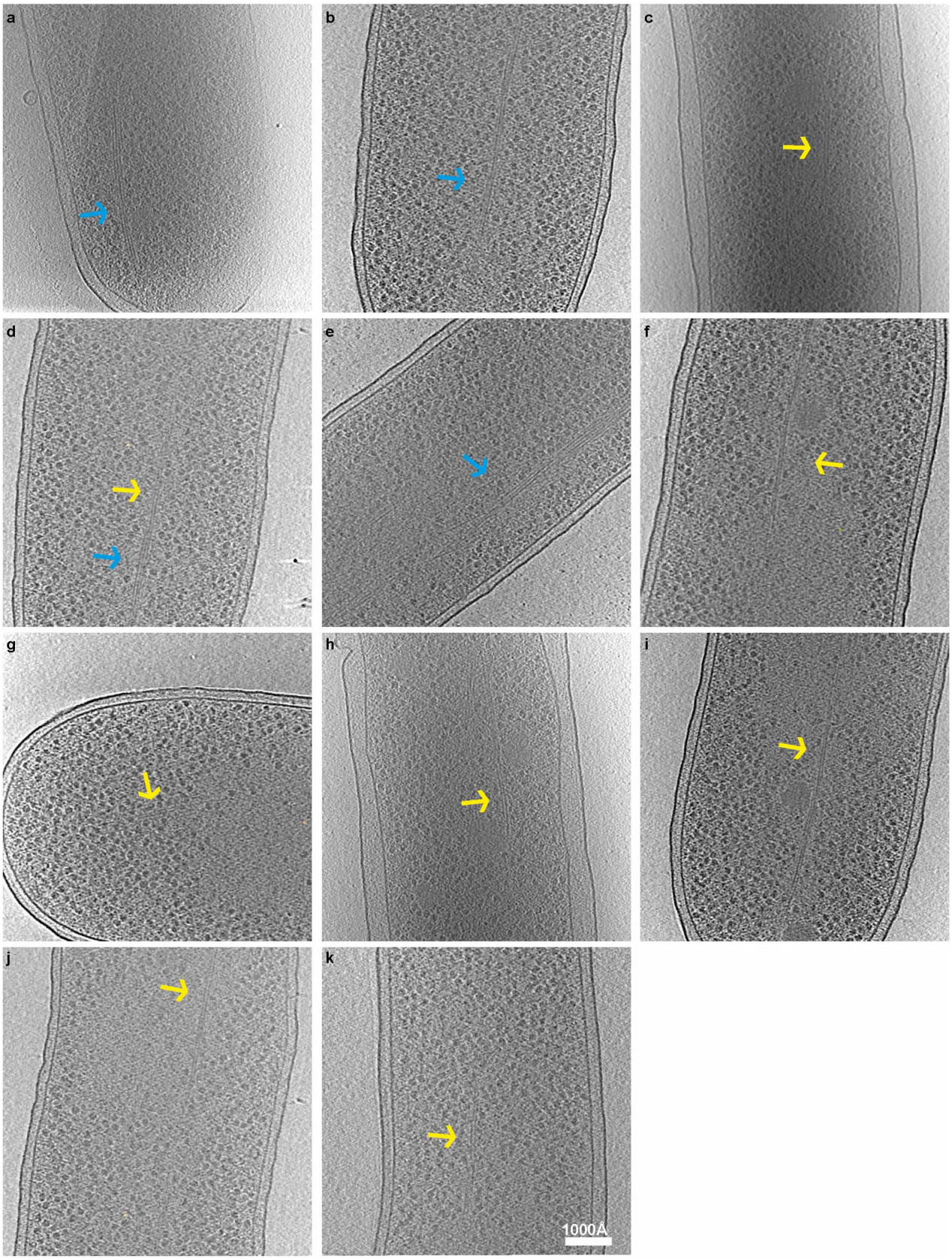

Extended Data Figure 7 | ParM bundles and doublets observed *in vivo*. **a**–**k**, *E. coli* B/R266 cells were transformed with a high-copy (pDD19) or medium-copy (pKG321) plasmid containing the ParMRC locus. Transformed cells were grown to log phase and then prepared for cryo-EM. This figure shows a gallery of ParM bundles (blue arrows) and doublets (yellow arrows) observed in these cells. **a**, **c**, **e**, **h**, Cells transformed with the high-copy-number plasmid; **b**, **d**, **f**, **g**, **i**, **j**, **k**, cells transformed with the medium-copy-number plasmid. Each experiment with different copy-number plasmids was performed only once owing to the low-throughput nature of cryo-ET.

Extended Data Table 1 | Image processing statistics for cryo-EM reconstructions of ParM filaments

	ParM+AMPPNP	ParM+ATP	ParM+ATP+ vanadate	ParM+ADP
Resolution, FSC at 0.143 (Å)	4.3	7.5	6.4	11.0
Filament pitch (Å)	54.0	54.0	53.8	51.0
Subunits per turn	2.18	2.18	2.18	2.18
Input segment step size (Å)	268	161	161	153
Segment size for alignment ($Å^2$)	364x364	400x400	400x400	700x700
Asymmetric units included	561,231	13,825	122,864	53,648

Extended Data Table 2 | Interfaces forming residues of ParM

Interface	Residue Numbers	Sequence
Inter-protofilament interface	1	MLVFIDDGSTNIKLQWQESDGTIKQHISPNSFKREWAVSFGDKKVFNYTLNGEQYSFDPI
	61	SPDAVVTTNIAWQYSDVNVVAVHHALLTSGLPVSEVDIVCTLPLTEYYDRNNQPNTENIE
	121	RKKANFRKKITLNGGDTFTIKDVKVMPESIPAGYEVLQELDELDSLLIIDLGGTTLDISQ
	181	VMGKLSGISKIYGDSSLGVSLVTSAVKDALSLARTKGSSYLADDIIIHRKDNNYLKQRIN
	241	DENKISIVTEAMNEALRKLEQRVLNTLNEFSGYTHVMVIGGGAELICDAVKKHTQIRDER
	301	FFKTNNSQYDLVNGMYLIGN
Intra-protofilament interface	1	MLVFIDDGSTNIKLQWQESDGTIKQHISPNSFKREWAVSFGDKKVFNYTLNGEQYSFDPI
	61	SPDAVVTTNIAWQYSDVNVVAVHHALLTSGLPVSEVDIVCTLPLTEYYDRNNQPNTENIE
	121	RKKANFRKKITLNGGDTFTIKDVKVMPESIPAGYEVLQELDELDSLLIIDLGGTTLDISQ
	181	VMGKLSGISKIYGDSSLGVSLVTSAVKDALSLARTKGSSYLADDIIIHRKDNNYLKQRIN
	241	DENKISIVTEAMNEALRKLEQRVLNTLNEFSGYTHVMVIGGGAELICDAVKKHTQIRDER
	301	FFKTNNSQYDLVNGMYLIGN
Inter-filament interface (doublet)	1	MLVFIDDGSTNIKLQWQESDGTIKQHISPNSFKREWAVSFGDKKVFNYTLNGEQYSFDPI
	61	SPDAVVTTNIAWQYSDVNVVAVHHALLTSGLPVSEVDIVCTLPLTEYYDRNNQPNTENIE
	121	RKKANFRKKITLNGGDTFTIKDVKVMPESIPAGYEVLQELDELDSLLIIDLGGTTLDISQ
	181	VMGKLSGISKIYGDSSLGVSLVTSAVKDALSLARTKGSSYLADDIIIHRKDNNYLKQRIN
	241	DENKISIVTEAMNEALRKLEQRVLNTLNEFSGYTHVMVIGGGAELICDAVKKHTQIRDER
	301	FFKTNNSQYDLVNGMYLIGN

Residues of ParM that are part of interfaces have been highlighted. Inter- and intra-protofilament interface-forming residues have been highlighted in red and green respectively. These residues have been assigned using a 4 Å distance cut-off based on the ParM+AMPPNP structure. Residues forming the inter-filament interface in the ParM doublet have been highlighted in blue. This assignment was based on a 7 Å distance cut-off for Cα atoms in the derived model of the ParM doublet because of the lower accuracy of the model.

Extended Data Table 3 | Instances of single, double and bundled ParM filaments seen in bacterial cells with different copy-number plasmids

Plasmid type	Single filaments	Double filaments	Bundles	Total number of cells imaged	Doublets per cell
High copy	5	35	8	6	5.83
Medium copy	11	36	2	23	1.56
Low copy	4	4	0	14	0.28

The ParMRC locus was inserted into high-, medium- and low-copy-number plasmids (plasmids pDD19, pKG321 and pKG491 respectively). These plasmids were in turn inserted into *E. coli* cells and imaged using cryo-ET. The ratio of observed doublets per cell (that is, the number of doublets observed divided by the number of cells imaged) was 5.8:1.6:0.3 (~19:5:1). These ratios are roughly the same as the expected copy-number ratios of the different copy-number plasmids.